Nano Research 2018, 11(6): 3222–3232
https://doi.org/10.1007/s12274-017-1851-5
Research Article
ISSN 1998-0124
CN 11-5974/O4

One-pot synthesis of Au@Pt star-like nanocrystals and their enhanced electrocatalytic performance for formic acid and ethanol oxidation

Yi Peng[1,2], Lidong Li[1] (✉), Ran Tao[1], Lingyu Tan[1], Mengna Qiu[1], and Lin Guo[1] (✉)

[1] *Key Laboratory of Bio-Inspired Smart Interfacial Science and Technology of Ministry of Education, School of Chemistry and Environment, Beihang University, Beijing 100191, China*
[2] *Department of Chemistry and Biochemistry, University of California, 1156 High Street, Santa Cruz, California 95064, USA*

Received: 13 April 2017
Revised: 6 September 2017
Accepted: 15 September 2017

KEYWORDS
Au@Pt core–shell nanocrystals,
electrocatalyst,
formic acid,
ethanol,
oxidation

ABSTRACT

The current bottleneck facing further developments in fuel cells is the lack of durable electrocatalysts with satisfactory activity. In this study, a simple and fast one-pot wet-chemical method is proposed to synthesize novel Au@Pt star-like bimetallic nanocrystals (Au@Pt SLNCs) with a low Pt/Au ratio of 1:4, which show great electrocatalytic properties and outstanding stability toward the electro-oxidation reactions commonly found in fuel cells. The star-like Au core (90 ± 20 nm) is partially coated with 5 nm Pt nanocluster shells, a morphology which creates a large amount of boundaries and edges, thus tuning the surface electronic structure as demonstrated by X-ray photoelectron spectroscopy and CO-stripping measurements. This promotes excellent electrocatalytic performance towards the formic acid oxidation reaction in acidic media and the ethanol oxidation reaction in alkaline media, compared to commercial Pt or Au@Pt triangular nanoprisms, in which the Au core is fully coated by a Pt shell. Au@Pt SLNCs have the highest current density within the dehydrogenation potential range, needing the least potential to achieve a certain current density as well as the highest long-term stability. Because of the small amount of Pt usage, very fast synthesis, excellent electrocatalytic activity and durability, the proposed Au@Pt SLNCs have a promising practical application in fuel cells.

1 Introduction

Proton exchange membrane fuel cells (PEMFCs) represent a clean and sustainable energy technology that has been attracting extensive interest in recent decades in which the operation of PEMFCs is generally involved. These systems involve the reduction of oxygen into water at the cathode and oxidation of small organic molecule fuels at the anode such as methanol, ethanol, and formic acid [1–6]. The development of

Address correspondence to Lidong Li, lilidong@buaa.edu.cn; Lin Guo, guolin@buaa.edu.cn

the anode oxidation reaction is limited by the lack of satisfactory electrocatalysts available. To date, the most state-of-the-art commercial electrocatalyst remains Pt/C, but the low supply and high cost as well as the relative poor durability of platinum are still major problems severely hampering wide-spread usage. Moreover, as the oxidation of these small molecule fuels on Pt surfaces always involves some the adsorted CO on the electrode surface (CO_{ads}) intermediate that can strongly bond to the Pt surface, the active sites of Pt can be easily poisoned during such reactions [7–11]. For instance, there are typically two pathways for the oxidation of formic acid: The so-called dehydrogenation in which HCOOH can be oxidized to CO_2 directly, or the dehydration process involving in CO_{ads} intermediate as HCOOH is first oxidized to CO [12–14]. Therefore, it is of both fundamental and technological significance to develop catalysts with lower Pt usage and enhanced activity, durability and poisoning tolerance. As for the ethanol oxidation reaction (which is more complicated), it is hindered by the slow and incomplete reaction pathway. This is because the reaction can generate several intermediates while the C–C bond cleavage is challenging. A high-index facet Pt was previously explored in order to break the C–C bonds and generate CO_2, but the synthesis of this Pt catalyst is still challenging [15, 16]. Another strategy is to alloy Pt with a second metal such as Pd, Ru, Sn, and Au [17–20]. Though some improvements have been made here, there is still no efficient catalyst for ethanol oxidation reaction available to date.

A variety of strategies have been adopted to solve these problems. For instance, one can increase the electrochemical surface area and lower the coordination number of metal centers by reducing the size of the nanocrystals [21–23]. Moreover, when the size is smaller than the Bohr radius, quantum confinement effects of electrons may lead to a discrete energy level distribution and a distinctive highest occupied molecular orbital (HOMO)–lowest unoccupied molecular orbital (LUMO) gap [24, 25]. On the other hand, the electronic structure of the catalysts is an essential factor that is highly related to the morphology, and thus the catalytic performance can be tuned by shape-controlled nanocrystals [15, 26–32]. Another significant approach is to optimize the lattice strain by means of adjusting the composition of multimetallic nanocrystals such as core–shell and/or alloy structures [33–37]. Nevertheless, it is still challenging to obtain electrocatalysts with long-term stability and excellent poisoning tolerance [38, 39].

Recently, Crooks et al. proposed that dendrimer-encapsulated Au@Pt nanoparticles (where the Au core is partially coated by Pt shell) exhibit better formic acid electro-oxidation activity and lower CO_{ads} formation which may attribute to the deformation of nanoparticle structure, slow dehydration of formic acid and weak binding of CO_{ads} [40]. This motivated us to design a new kind of Au@Pt core–shell bimetallic nanocrystal with better electrocatalytic performance and CO_{ads} tolerance. Herein, we report a facile and fast one-pot wet chemical approach to synthesize Au@Pt star-like bimetallic nanocrystals (SLNCs) that the Au cores are partially coated by Pt nanoclusters as evidenced by X-ray photoelectron spectroscopy (XPS) and cyclic voltammetry (CV). The proposed Au@Pt SLNCs shows much better formic acid oxidation reaction (FAOR) and ethanol oxidation reaction (EOR) performance and CO_{ads} tolerance compared with complete Pt coated Au@Pt triangular core–shell bimetallic nanoprisms (Au@Pt TANPs). Furthermore, the amount of H_2PtCl_6 in the precursors is only one fourth that of $HAuCl_4$, reducing the overall reagent cost. Based on the advantages of low Pt loading, low operation potential, high CO_{ads} tolerance and fast synthesis process, the Au@Pt SLNPs have great potential applications as anode electrocatalysts in PEMFCs.

2 Results and discussion

For the typical synthesis of the Au@Pt SLNCs, a solution with a 4:1 molar ratio of $HAuCl_4/H_2PtCl_6$ was co-reduced by ascorbic acid in the polyvinylpyrrolidone (PVP) and didodecyldimethylammonium bromide (DDAB) binary surfactant system. The products were obtained after 1 h heating at 80 °C and purified by water and ethanol (see details in Experimental section). Scanning electron microscopy (SEM) imaging (Fig. S1 in the Electronic Supplementary Material (ESM)) showed that the size of the nanocrystals is approximately 95 ± 20 nm based on more than 100 well-dispersed particles. Figure 1(a) shows

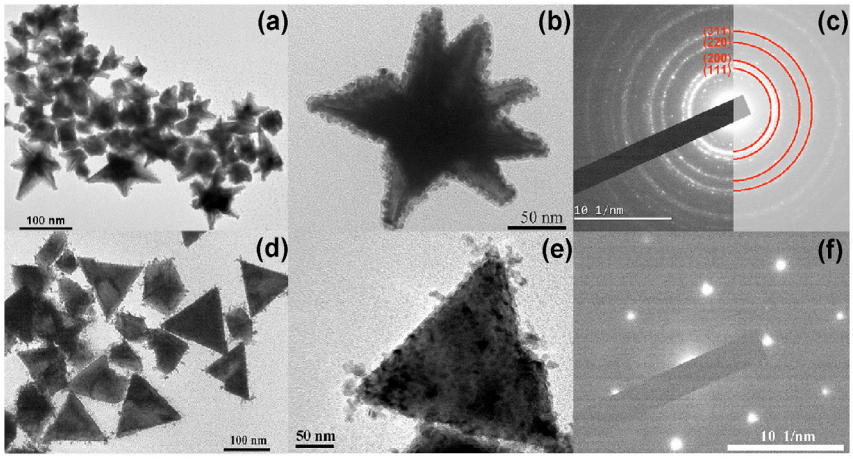

Figure 1 Morphology and structure of as-prepared Au@Pt SLNCs synthesized in the presence of silver ions (a)–(c) and Au@Pt TANPs (d)–(f) synthesized without silver ions as a control sample. (a) and (d) are TEM images. (b) and (e) are TEM images of single particles. (c) and (f) Corresponding SAED patterns.

the well-defined star-like structure of the nanocrystals, and a transmission electron microscopy (TEM) image of a single particle (Fig. 1(b)) indicates that the star-like gold core is coated by a 5.5 nm-thick Pt nanocluster shell. The clearly-observed domain boundaries reveal the polycrystalline nature of the Au@Pt SLNCs. This is consistent with the selected area electron diffraction (SAED) pattern of a single Au@Pt SLNC, which shows concentric rings composed of bright elongated spots and is well-indexed to a polycrystalline structure of primary nanoclusters with a face center cubic (fcc) structure [41, 42]. In contrast, without the presence of silver ions during synthesis, the obtained product was triangular nanoprisms as shown in Figs. 1(d) and 1(e). The corresponding SAED pattern shown in Fig. 1(f) with a (111) orientation indicates the single-crystal nature of the Au@Pt TANPs, exhibiting six bright spots to form a regular hexagon that is highly consistent with fcc single crystal SAED patterns [43, 44]. This indicates that the gold core is completely coated by a full Pt shell with a single-crystal nature.

To investigate the morphological evolution of the Au@Pt SLNCs, UV–Vis and TEM measurements were taken from products sampled at different reaction times. The UV–Vis spectra shown in Fig. S2 in the ESM indicate that the reaction solution did not show any absorbance peak before heating. When heated to 80 ˚C, an absorbance peak appeared at approximately 570 nm corresponding to the well-known surface plasmon resonance (SPR) of gold nanocrystals, which increased gradually over time because of the nucleation of the earlier-reduced gold atoms [45]. The absorbance reached its maximum at 15 min, as reflected in the finalization of the growth of gold core. Next, the absorbance began to decrease and shift to higher wavelengths as the later-reduced platinum sequentially grew on the gold core surface to block the gold nanocrystal SPR. Finally, the absorbance stabilized at 30 min without further changes even after heating for 60 min. Furthermore, the TEM images in Figs. 2(a)–2(c) show the morphologies of the nanocrystal at different reaction stages. A high yield quasi star-like structure was observed at 8 min and the star-like core was completely formed after 15 min. The star-like core was coated by separating dispersed Pt nanoclusters to form a partially coated Pt shell on the gold core surface. Based on this evidence, a schematic diagram of the growth process is given in Fig. 2(d) that the reduced gold atoms first nucleated and then grew to form quasi star-like Au cores. The Pt atoms reduced later and further grew on the Au cores to form partial Pt shell coatings.

High resolution transmission electron microscopy (HRTEM) measurements were employed to further study the surface structures of the Au@Pt SLNCs, as shown in Fig. 3. The higher-magnification TEM image in Fig. 3(a) depicts a star-like gold core with Pt nanoclusters forming a shell, and the boxed regions were further examined by HRTEM (Figs. 3(b)–3(d)). Notably, well-defined spacing lattice fringes with distances of 2.26, 1.96 and 1.38 Å were found in the HRTEM images

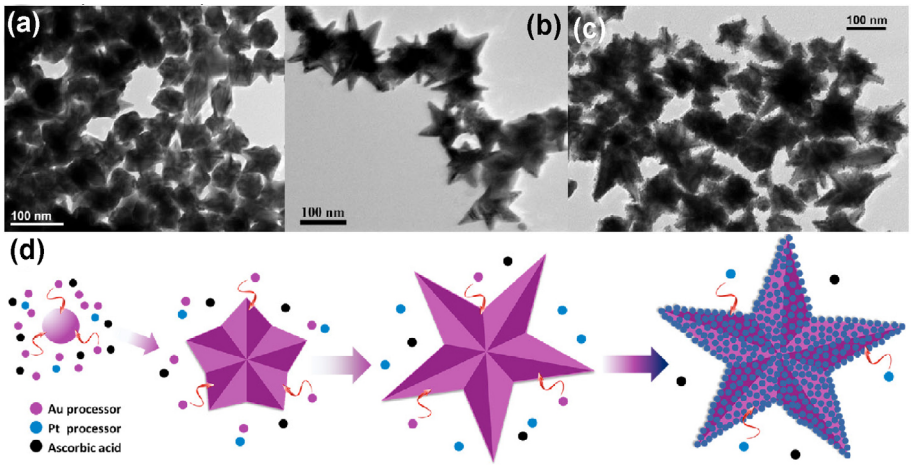

Figure 2 (a)–(c) TEM images of Au@Pt SLNCs sampled at different stages during synthesis. (a) 5, (b) 15, and (c) 30 min. (d) Schematic diagram of the growth process.

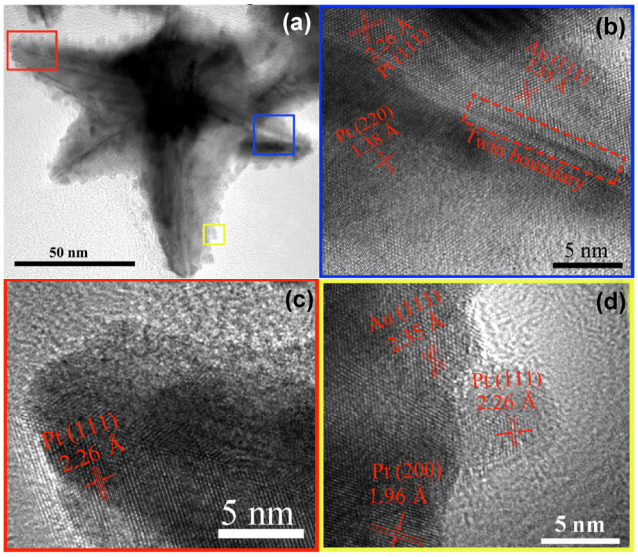

Figure 3 (a) TEM image of a Au@Pt SLNC. (b)–(d) HRTEM images of the boxed regions in (a).

as marked, which correspond to the interplanar distances of Pt {111}, {200} and {220} facets respectively [46, 47]. This further confirmed the polycrystalline nature of the Au@Pt SLNCs, which is consistent with the SAED pattern. Another fringe distance of 2.35 Å which can be assigned to the Au {111} facet is also present [48], demonstrating the previous claim that the Au core is partially coated by a Pt nanocluster shell. However, only the Pt {111} facet was present (Fig. S3 in the ESM) on the surface of Au@Pt TANPs synthesized without silver ions, indicating that the gold core is fully coated by a single crystalline Pt shell which is consistent with previous claims.

Figure 4(a) shows the XPS survey spectra and binding energies for Au 4f, Pt 4f and Ag 3d presented as labeled for the Au@Pt SLNCs, while only binding energies of Au 4f and Pt 4f were presented for the Au@Pt TANPs. These results are in good agreement with the results from an SEM image of a corner of Au@Pt SLNC and Au@Pt TANP (Fig. S4 in the ESM). Figure 4(b) depicts high-resolution XPS spectra of the two samples in the Ag 3d range. Strong peaks of Ag $3d_{5/2}$ and Ag $3d_{3/2}$ at 367.8 and 373.8 eV were observed for Au@Pt SLNCs [49], whereas no signals of Ag 3d can be found at the same position for the Au@Pt TANPs. Based on this information, the silver ions are significant for the formation of Au@Pt SLNC structures that the star-like Au core is partially coated by a Pt nanocluster shells. Figure S5 in the ESM schematically displays the formation mechanism of star-like or triangular structures in the presence and absence of silver ions. In brief, the gold ions were initially reduced to form seeds, which continued to grow to form quasi-triangular nanoprisms in the presence of PVP and DDAB surfactants [50]. In the absence of silver ions, the quasi-triangular nanoprisms would simply continue to grow and form Au@Pt TANPs (Fig. 1(d)). Silver ions can be reduced by ascorbic acid in the presence of gold ions and form an under-potential deposition (UPD) atomic layer on the former nucleated gold surface as investigated by Chad et al. [51, 52]. As the silver ions are limited, the UPD atomic layer cannot fully coat the gold surface. As the Ag UPD

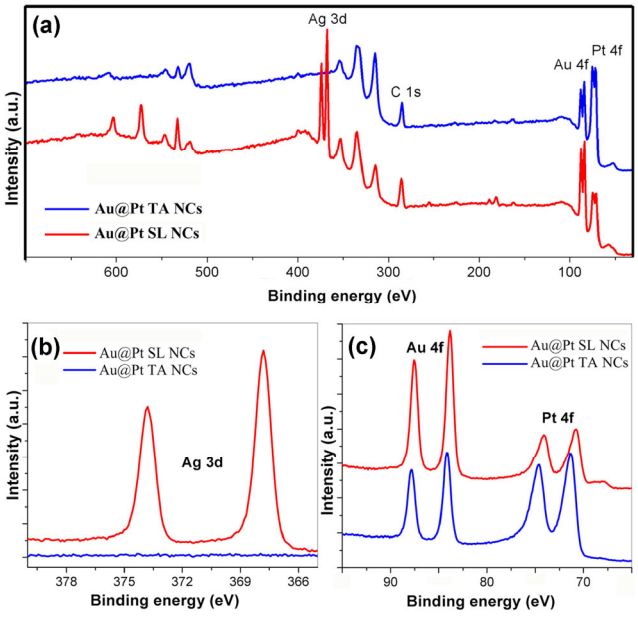

Figure 4 XPS spectra of the as-prepared Au@Pt SLNCs (red lines) and the referenced Au@Pt TANPs (blue lines). (a) XPS survey spectra. (b) High-resolution XPS spectra of Ag 3d. (c) High resolution XPS spectra of Au 4f and Pt 4f.

layer on the gold surface cannot be easily removed, it can efficiently slow the growth rate of surrounding regions, thus the growth rates along different orientations of the seeds are heterogeneous and anisotropic as Au@Pt SLNCs are produced (Fig. 1(a)). In addition, a control experiment was carried out to test the effect of Ag ion addition to the star-like structure (as shown in Fig. S6 in the ESM). As the amount of silver ions increases, the anisotropic growth becomes more and more obvious.

Furthermore, Fig. 4(c) shows the high-resolution XPS spectra of the two samples in the Au 4f and Pt 4f ranges. For Au@Pt SLNCs, the core level binding energies are 70.85 and 74.18 eV for Pt $4f_{7/2}$ and Pt $4f_{5/2}$, respectively, and 83.86 and 87.54 eV for Au $4f_{7/2}$ and Au $4f_{5/2}$, respectively. For Au@Pt TANPs, the core level binding energies are 71.30 and 74.63 eV for Pt $4f_{7/2}$ and Pt $4f_{5/2}$, respectively, and 84.10 and 87.77 eV for Au $4f_{7/2}$ and Au $4f_{5/2}$, respectively. The Au/Pt atomic ratios were 1.52 and 0.53 for Au@Pt SLNCs and Au@Pt TANPs, respectively. The relative Au/Pt atomic ratios account for the formation of Au@Pt core–shell structures, which facilitates the attenuation of photoelectrons escaping from the Au core [53]. Note that the penetration depth for XPS measurements is typically in the range of a few nanometers, so the much higher Au/Pt atomic ratio of Au@Pt SLNCs (compared to Au@Pt TANPs) further confirm that Au@Pt SLNCs are partially coated by a Pt shell, as the Pt shell thickness is a similar length scale. Of note, the binding energies of Pt $4f_{7/2}$ of Au@Pt SLNCs and Au@Pt TANPs were 0.47 and 0.06 eV lower than that of pure Pt as reported in the literature (71.32 eV) [54]. This is attributed to the intraparticle charge transfer from Au core to Pt shell which tunes the surface electronic structure. Similar results were observed in nanocomposites of Ag_2S and noble metals [55]. The greater shift of Au@Pt SLNCs is attributed to the stronger interaction of Au core and Pt shell, as the partially Pt coated surface structure can provide a large number of Au–Pt boundaries and thus increase the edges with lower coordination numbers and change the surface lattice strain [56, 57].

Since the XPS and TEM measurements are limited by the capability of differentiating surface Au and Pt atoms, cyclic voltammetry (CV) was also used to measure the surface composition of the Au@Pt samples. Figure 5 shows typical CV curves of the Au@Pt SLNCs and Au@Pt TANPs between –0.2 – 1.5 V (vs. Ag/AgCl) in 0.5 M H_2SO_4 solution. The Au oxide reduction peak at ~ 0.85 V can be observed for Au@Pt SLNCs, but is not observed for Au@Pt TANPs. Furthermore, the Pt oxide reduction peak of Au@Pt SLNCs appear at approximately 0.37 V while the peak of Au@Pt TANPs is approximately 0.43 V. The 0.06 V lower reduction potential difference indicates the higher electrochemical activity of Au@Pt SLNCs, which may be attributed to the tuning of the surface electronic structures due to the unique surface structures, consistent with the observed negative shift of the Pt $4f_{7/2}$ binding energy. When assuming that a charge of 400 and 440 $\mu C \cdot cm^{-2}$ is required to reduce Au oxide and Pt oxide respectively [58, 59], the surface area of Au/Pt of Au@Pt SLNCs can be established as 0.97 which is relatively smaller than the result based on XPS measurement (Au/Pt = 1.52), as only the surface atoms were counted when using this electrochemistry method. This directly demonstrates the claim that Au@Pt SLNCs are partially coated by Pt while Au@Pt TANPs are fully coated by Pt, consistent with the TEM and XPS measurements.

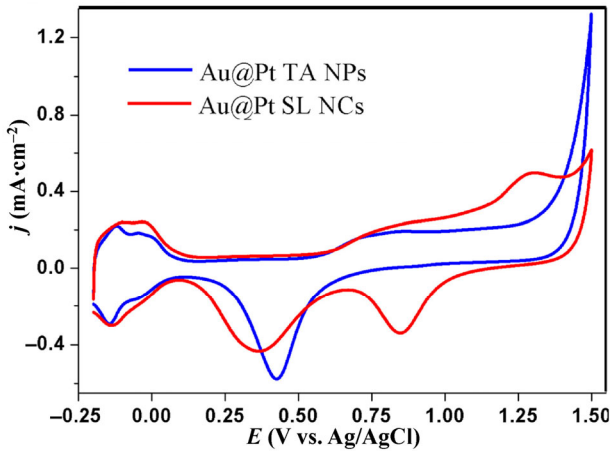

Figure 5 CV curves of the Au@Pt SLNCs and Au@Pt TANPs from –0.2 to 1.5 V obtained in a N_2-saturated electrolyte solution containing 0.5 M H_2SO_4. The scanning rate is 50 mV·s^{-1} and the current densities are normalized by the electrochemical active surface activity.

To test the electrocatalytic properties of this system, the electrochemical active surface area (ECSA) was measured in a 0.5 M H_2SO_4 solution with a scan rate of 50 mV·s^{-1} from –0.2 V to 1 V (vs. Ag/AgCl). According to the CV curves in Fig. S7 in the ESM, the ECSA was estimated as 52.7, 36.6 and 29.7 m^2·g^{-1} for Au@Pt SLNCs, Au@Pt TANPs and commercial Pt/C, respectively.

Figures 6(a)–6(d) depict the FAOR performance in N_2-saturated electrolyte solution containing 0.5 M HCOOH and 0.5 M H_2SO_4. In Fig. 6(a), there are two forward scanning peaks at 0.32 and 0.7 V, where the first peak is associated with the dehydrogenation (direct reaction) pathway and the second one is associated with the dehydration (indirect reaction) pathway [60, 61]. The current density ratios of indirect and direct reactions are ~ 1.99 and ~ 5.72 for the Au@Pt TANPs and the commercial Pt/C, respectively, indicating that there are more indirect reactions occurring at the commercial Pt/C surface than Au@Pt TANPs. There is no apparent peak near 0.7 V for Au@Pt SLNCs, suggesting that no indirect reactions occurred at the Au@Pt SLNCs. The low current density ratio of Au@Pt SLNCs when backward scanning to forward scanning (0.97), compared to Au@Pt TANPs (6.6) and commercial Pt/C (10.3), is consistent with the result that the dominant pathway of FAOR on the Au@Pt SLNCs surface is dehydrogenation. The atomic arrangement must be taken into consideration to explain this behavior. At least three neighboring Pt atoms are needed for the dehydration pathway, which means that the continuous Pt surface is favorable for the dissociative adsorption of formic acid to form CO_{ads} [62]. While only one Pt site is required for the dehydrogenation pathway, which suggested that the discontinuous Pt surface overlayers on Au can efficiently decrease the availability of adjacent Pt atoms, suppressing the dehydration rate and thus blocking CO_{ads} formation [63]. Besides, the current density of the direct reaction of the proposed Au@Pt SLNCs is 8.12 mA·cm^{-2} which is ~ 5.24 and 25.37 times higher than that of Au@Pt TANPs and commercial Pt/C, respectively, also indicating dramatic improvement of the Au@Pt SLNCs activity. When normalized by the mass of Pt, the mass activity of Au@Pt SLNCs is 4.28 A·mg^{-1}, which is ~ 7.55 and 45 times higher than that of Au@Pt TANPs and commercial Pt/C, respectively. The enhanced factor of Au@Pt SLNCs is even better than specific activity (Fig. 6(b)). Figure 6(c) shows zoomed-in areas at lower potentials, showing that the potential needs to reach a current density of 0.25 mA·cm^{-2} are –54 (Au@Pt SLNCs), +93 (Au@Pt TANPs) and +230 mV (commercial Pt/C). These results also suggest that the FAOR is more efficient on Au@Pt SLNC surfaces. As the CO_{ads} is involved in the indirect reaction pathway which may poison the active Pt sites and slow down the reaction rate, the long-term stability of the electrocatalysts becomes rather significant for the fuel cells. Figure 6(d) shows the *j*–*t* curves and the current density at 60 min (fixed potential of 0.32 V) is 2.02 mA·cm^{-2} for Au@Pt SLNCs, 14.8 and 147 times higher than that of Au@Pt TANPs and commercial Pt, indicating Au@Pt SLNCs has the highest electrocatalytic long-term stability toward FAOR. This is consistent with the long-term poisoning rate (δ) calculated as [64, 65]

$$\delta\,(\%\cdot s^{-1}) = \frac{100}{I_0} \times \left(\frac{dI}{dt}\right)_{t>500s}$$

where $(dI/dt)_{t>500s}$ is the slope of the linear portion of the current decay, and I_0 is the current at the start of polarization back-extrapolated from the linear current decay. The poisoning rate was calculated as 0.021, 0.054

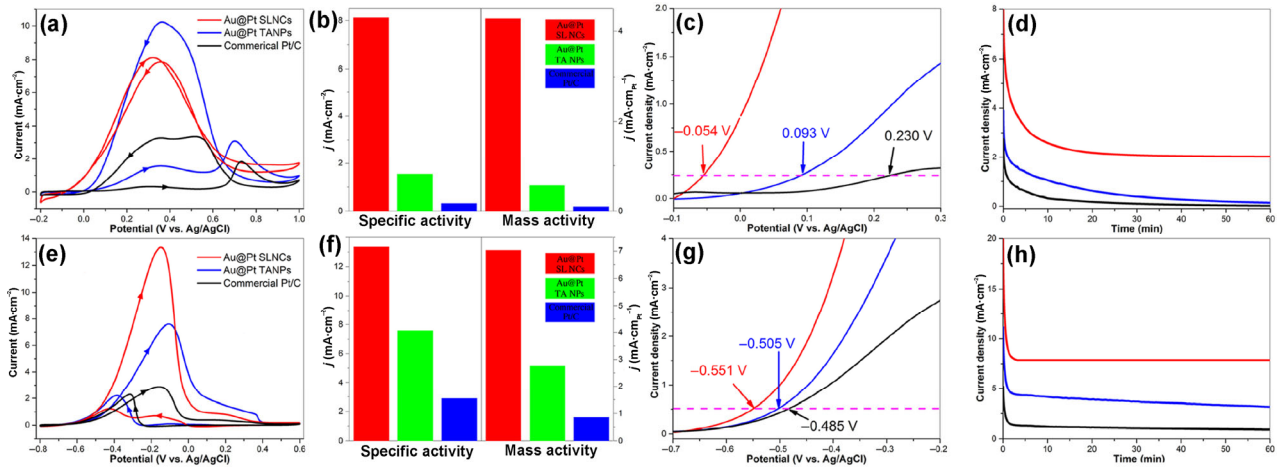

Figure 6 The electrocatalytic performances of Au@Pt SLNCs (red lines), Au@Pt TANPs (blue lines) and commercial Pt/C (black lines) toward FAOR in the N_2-saturated electrolyte solution containing 0.5 M HCOOH and 0.5 M H_2SO_4 (a)–(d) and EOR in the N_2-saturated electrolyte solution containing 0.5 M C_2H_5OH and 0.5 M KOH (e)–(h). (a) Typical CV curves of FAOR with different catalysts. (b) FAOR specific and mass activity comparisons. (c) Zoomed-in curves of (a). (d) Current density vs. time curves for different catalysts under a fixed potential of 0.32 V for FAOR. (e) Typical CV curves of EOR with different catalysts. (f) EOR specific and mass activity comparisons. (g) Zoomed-in curves of (a). (h) Current density vs. time curves for different catalysts under a fixed potential of −0.15 V for EOR.

and 0.105 %·s^{-1} for Au@Pt SLNCs, Au@Pt TANPs and commercial Pt/C, respectively.

Similarly, the electrocatalytic activities toward EOR were measured in N_2-saturated electrolyte solution containing 0.5 M C_2H_5OH and 0.5 M KOH. The oxidation peak current density of Au@Pt SLNCs (13.34 mA·cm^{-2}) is 1.76 and 4.63 times higher than that of Au@Pt TANPs and commercial Pt/C (Fig. 6(e)), respectively. When normalized by the mass of Pt, the mass activity of Au@Pt SLNCs is 7.03 A·mg^{-1}, which is ~ 2.53 and 8.22 times higher than that of Au@Pt TANPs and commercial Pt/C, respectively. The enhanced factor of Au@Pt SLNCs is even better than the specific activity (Fig. 6(f)). The potentials needed to achieve a current density of 0.5 mA·cm^{-1} are –0.551, –0.505, and –0.485 V for Au@Pt SLNCs, Au@Pt TANPs and commercial Pt/C, respectively (Fig. 6(g)). These two comparisons suggest that the Au@Pt SLNCs have the best electrocatalytic activity toward ethanol oxidation. Figure 6(h) further depicted the *j*–*t* curves and the current density at 60 min (fixed potential of –0.15 V) is 7.85 mA·cm^{-2} for Au@Pt SLNCs, which is 2.49 and 8.74 times higher than that of Au@Pt TANPs and commercial Pt/C respectively, indicating that Au@Pt SLNCs have the highest catalytic long-term stability toward EOR. Correspondingly, the poisoning rates were 0.007 %·s^{-1} (Au@Pt SLNCs), 0.093 %·s^{-1} (Au@Pt TANPs) and 0.128 %·s^{-1} (commercial Pt/C).

Based on the above discussion, the improved activity and long-term stability of the electrocatalytic performance of Au@Pt SLNCs may be attributed to the change of the surface electronic structure which may lead a d-band center shift [66, 67]. To probe the variation in d-band center caused by the electronic coupling between Au and Pt, CO-stripping measurements were conducted by holding in 0.5 M H_2SO_4 solution with CO bubbling for 20 min to absorb CO on the surface of the electrocatalysts, and the absorbed CO was removed by electrochemical CV scanning under N_2; the corresponding first CV scan curves are depicted in Fig. 7. The commercial Pt/C shows a maximum CO oxidation peak at 0.70 V, which suggests a strong CO adsorption on the Pt surface. The CO oxidation peaks of Au@Pt SLNCs and Au@Pt TANPs are centered at 0.60 and 0.63 V respectively, which are relatively lower than that of the commercial Pt/C, thus indicating weaker CO adsorption. The CO-stripping shift can be accounted for by the electronic coupling between Au and Pt and the larger shift of Au@Pt SLNCs indicates a more efficient electronic coupling. This observation is highly consistent with the XPS measurement where Au@Pt SLNCs have a

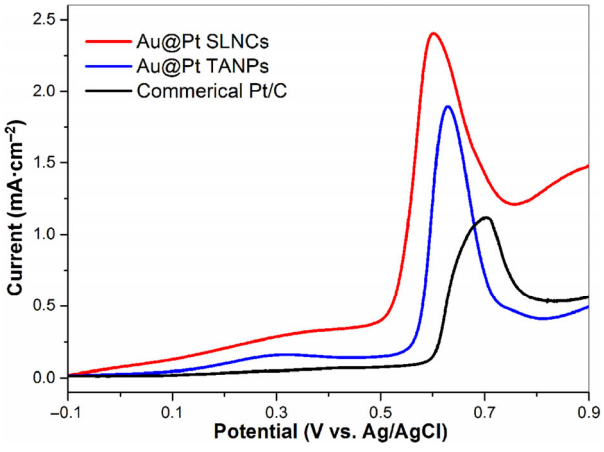

Figure 7 CO stripping voltammograms of Au@Pt SLNCs (red lines), Au@Pt TANPs (blue lines) and commercial Pt/C (black lines) in CO saturated electrolyte solution containing 0.5 M H_2SO_4.

more negative Pt $4f_{7/2}$ shift (0.43 eV) compared to Au@Pt TANPs, and the electrocatalytic performance shows that the Au@Pt SLNCs have the best activity and long-term stability compared to Au@Pt TANPs and commercial Pt/C.

3 Experimental section

3.1 Chemicals

Tetrachloroauric acid ($HAuCl_4·4H_2O$, 99.9%, Alfa-Aesar), hexachloroplatinic acid ($H_2PtCl_6·6H_2O$, 99.9%, Alfa-Aesar), PVP (M_W = 58,000, Alfa-Aesar), DDAB (99%, Alfa-Aesar), L-ascorbic acid (AA, 99%, J&K Scientific), and silver nitrate ($AgNO_3$, 99%, Alfa-Aesar) were used without further purification. Other chemical reagents were analytically pure and purchased from Beijing Chemical Works. All water used during the experiment was deionized water.

3.2 Synthesis of Au@Pt bimetallic nanocrystals

In a typical synthesis, 5 mL aqueous solution containing 40 g·L^{-1} PVP and 10 mmol·L^{-1} DDAB was mixed with 4 mL $HAuCl_4$ (1 mM) and 1 mL H_2PtCl_6 (1 mM). Afterwards, 100 μL $AgNO_3$ (0.01 M), 200 μL AA (0.2 M) and 100 μL HCl (0.01 M) were added to the solution to form a homogenous solution. To synthesize Au@Pt SLNCs, the above solution was heated to 80 °C and kept for 1 h, and then quickly cooled in ice-cold water. To synthesize the control sample (Au@Pt TANPs), the same procedures were used but without the addition of $AgNO_3$. Excess surfactants were rinsed by deionized water and ethanol five times to obtain the purified product.

3.3 Characterization

UV–vis spectra were collected using a UV-vis spectrophotometer at different times without any further solution purification. The morphologies and structures of the washed products were further characterized by SEM (JEOL JSM-7500F), TEM (JEOL JEM-2010) and HRTEM (JEOL JEM-2010F). XPS measurements were carried out on an Axis Ultra spectrometer at a pressure < 10^{-8} Torr with a standard Al Kα excitation source (1,486.6 eV) and calibrated to the binding energy of C 1s peak at 284.8 eV.

3.4 Electrochemical measurements

CV and chronoamperometry (CA) measurements were carried out on a CHI 660C electrochemical workstation (Chenhua, Shanghai) at room temperature. Prior to catalyst loading, the glass carbon electrode (GCE, d = 2 mm) was polished with alumina powder to a mirror finish and washed thoroughly with deionized water. The working electrodes were fabricated by dropcast 10 μL Au@Pt NPs (2 mg·mL^{-1}) onto GCE. Pt wire and Ag/AgCl (in saturated NaCl) were used as the counter and reference electrodes, respectively. The electro-catalyst modified GCE was coated by 5 μL Nafion solution (0.05 wt.%) and dried at room temperature. The dried GCE was cleaned again by washing with water and then electrochemically cleaned by potential cycles at a scan rate of 50 mV·s^{-1} between –0.20 and 1.50 V vs. Ag/AgCl in 0.5 M H_2SO_4. The electrolyte solutions were purged with high-purity N_2 gas before use for approximately 0.5 h. FAOR was carried out in an aqueous solution of 0.5 M H_2SO_4 and 0.5 M formic acid. EOR was measured in an aqueous solution of 0.5 M KOH and 0.5 M ethanol. CO stripping was carried out by saturating 0.5 M H_2SO_4 with 10% CO in Ar, and voltammograms were collected at a potential range of –0.2 to 1.5 V (starting from –0.1 V).

4 Conclusions

We have developed a facile one-pot aqueous synthesis

process for the production of Au@Pt core–shell bimetallic nanocrystals in a PVP/DDAB binary surfactant system. The nanocrystal structure is a star-like Au core and a non-contiguous thin Pt shell formed by Pt nanoclusters, as confirmed by HRTEM, XPS, and electrochemical characterizations. Silver ions were essential for the structure formation owing to the silver UPD that slowed the growth rate in a certain direction. The proposed Au@Pt SLNCs exhibited enhanced electrocatalytic performance for FAOR and EOR as the proposed catalyst has low operating potential as well as high current density. More interestingly, for FAOR, dehydrogenation is the dominant pathway which can avoid active site poisoning by CO_{ads} for improved long-term stability. This can be ascribed to the partial Pt coated structure providing plenty of Au–Pt boundaries for strong interactions between Au and Pt and strong surface electronic structure changes. This may provide some insight for future electrocatalyst design and material synthesis, and our system also has potential for practical use in PEMFCs.

Acknowledgements

This work was financially supported by the National Natural Science Foundation of China (No. 21273001) and the National Basic Research Program of China (No. 2014CB931802).

Electronic Supplementary Material: Supplementary material is available in the online version of this article at https://doi.org/10.1007/s12274-017-1851-5.

References

[1] Sharaf, O. Z.; Orhan, M. F. An overview of fuel cell technology: Fundamentals and applications. *Renew. Sust. Energ. Rev.* **2014**, *32*, 810–853.

[2] Peng, Y.; Lu, B. Z.; Wang, N.; Li, L. G.; Chen, S. W. Impacts of interfacial charge transfer on nanoparticle electrocatalytic activity towards oxygen reduction. *Phys. Chem. Chem. Phys.* **2017**, *19*, 9336–9348.

[3] Stamenkovic, V. R.; Strmcnik, D.; Lopes, P. P.; Markovic, N. M. Energy and fuels from electrochemical interfaces. *Nat. Mater.* **2017**, *16*, 57–69.

[4] Sui, S.; Wang, X. Y.; Zhou, X. T.; Su, Y. H.; Riffatc, S.; Liu, C. J. A comprehensive review of Pt electrocatalysts for the oxygen reduction reaction: Nanostructure, activity, mechanism and carbon support in PEM fuel cells. *J. Mater. Chem. A* **2017**, *5*, 1808–1825.

[5] Sheng, T.; Xu, Y. F.; Jiang, Y. X.; Huang, L.; Tian, N.; Zhou, Z. Y.; Broadwell, I.; Sun, S. G. Structure design and performance tuning of nanomaterials for electrochemical energy conversion and storage. *Acc. Chem. Res.* **2016**, *49*, 2569–2577.

[6] Zhu, C. Z.; Du, D.; Eychmuller, A.; Lin, Y. H. Engineering ordered and nonordered porous noble metal nanostructures: Synthesis, assembly, and their applications in electrochemistry. *Chem. Rev.* **2015**, *115*, 8896–8943.

[7] Chen, Y. X.; Heinen, M.; Jusys, Z.; Behm, R. J. Bridge-bonded formate: Active intermediate or spectator species in formic acid oxidation on a Pt film electrode? *Langmuir* **2006**, *22*, 10399–10408.

[8] Cuesta, A. At least three contiguous atoms are necessary for CO formation during methanol electrooxidation on platinum. *J. Am. Chem. Soc.* **2006**, *128*, 13332–13333.

[9] Cuesta, A.; Cabello, G.; Gutiérrez, C.; Osawa, M. Adsorbed formate: The key intermediate in the oxidation of formic acid on platinum electrodes. *Phys. Chem. Chem. Phys.* **2011**, *13*, 20091–20095.

[10] Herrero, E.; Fernández-Vega, A.; Feliu, J. M.; Aldaz, A. Poison formation reaction from formic acid and methanol on Pt(111) electrodes modified by irreversibly adsorbed Bi and As. *J. Electroanal. Chem.* **1993**, *350*, 73–88.

[11] Sun, S. G.; Clavilier, J. Electrochemical study on the poisoning intermediate formed from methanol dissociation at low index and stepped platinum surfaces. *J. Electroanal. Chem.* **1987**, *236*, 95–112.

[12] Wang, S. Y.; Kristian, N.; Jiang, S. P.; Wang, X. Controlled deposition of Pt on Au nanorods and their catalytic activity towards formic acid oxidation. *Electrochem. Commun.* **2008**, *10*, 961–964.

[13] Zhang, S.; Shao, Y. Y.; Liao, H. G.; Liu, J.; Aksay, I. A.; Yin, G. P.; Lin, Y. H. Graphene decorated with PtAu alloy nanoparticles: Facile synthesis and promising application for formic acid oxidation. *Chem. Mater.* **2011**, *23*, 1079–1081.

[14] Zhang, S.; Shao, Y. Y.; Yin, G. P.; Lin, Y. H. Electrostatic self-assembly of a Pt-around-Au nanocomposite with high activity towards formic acid oxidation. *Angew. Chem., Int. Ed.* **2010**, *49*, 2211–2214.

[15] Tian, N.; Zhou, Z. Y.; Sun, S. G.; Ding, Y.; Wang, Z. L. Synthesis of tetrahexahedral platinum nanocrystals with high-index facets and high electro-oxidation activity. *Science* **2007**, *316*, 732–735.

[16] Zhou, Z. Y.; Huang, Z. Z.; Chen, D. J.; Wang, Q.; Tian, N.;

Sun, S. G. High-index faceted platinum nanocrystals supported on carbon black as highly efficient catalysts for ethanol electrooxidation. *Angew. Chem., Int. Ed.* **2010**, *49*, 411–414.

[17] Colmati, F.; Antolini, E.; Gonzalez, E. R. Effect of temperature on the mechanism of ethanol oxidation on carbon supported Pt, PtRu and Pt_3Sn electrocatalysts. *J. Power Sources* **2006**, *157*, 98–103.

[18] Dong, L. F.; Gari, R. R. S.; Li, Z.; Craig, M. M.; Hou, S. F. Graphene-supported platinum and platinum-ruthenium nanoparticles with high electrocatalytic activity for methanol and ethanol oxidation. *Carbon* **2010**, *48*, 781–787.

[19] Dutta, A.; Mahapatra, S. S.; Datta, J. High performance PtPdAu nano-catalyst for ethanol oxidation in alkaline media for fuel cell applications. *Int. J. Hydrogen Energ.* **2011**, *36*, 14898–14906.

[20] Ren, F. F.; Wang, H. W.; Zhai, C. Y.; Zhu, M. S.; Yue, R. R.; Du, Y. K.; Yang, P.; Xu, J. K.; Lu, W. S. Clean method for the synthesis of reduced graphene oxide-supported PtPd alloys with high electrocatalytic activity for ethanol oxidation in alkaline medium. *ACS Appl. Mater. Interfaces* **2014**, *6*, 3607–3614.

[21] Shao, M. H.; Peles, A.; Shoemaker, K. Electrocatalysis on platinum nanoparticles: Particle size effect on oxygen reduction reaction activity. *Nano Lett.* **2011**, *11*, 3714–3719.

[22] Yang, X. F.; Wang, A. Q.; Qiao, B. T.; Li, J.; Liu, J. Y.; Zhang, T. Single-atom catalysts: A new frontier in heterogeneous catalysis. *Acc. Chem. Res.* **2013**, *46*, 1740–1748.

[23] Gan, L.; Rudi, S.; Cui, C. H.; Heggen, M.; Strasser, P. Size-controlled synthesis of sub-10 nm $PtNi_3$ alloy nanoparticles and their unusual volcano-shaped size effect on ORR electrocatalysis. *Small* **2016**, *12*, 3189–3196.

[24] Valden, M.; Lai, X.; Goodman, D. W. Onset of catalytic activity of gold clusters on titania with the appearance of nonmetallic properties. *Science* **1998**, *281*, 1647–1650.

[25] Li, J.; Li, X.; Zhai, H. J.; Wang, L. S. Au_{20}: A tetrahedral cluster. *Science* **2003**, *299*, 864–867.

[26] Xia, Y. N.; Xiong, Y. J.; Lim, B.; Skrabalak, S. E. Shape-controlled synthesis of metal nanocrystals: Simple chemistry meets complex physics? *Angew. Chem., Int. Ed.* **2009**, *48*, 60–103.

[27] Chen, M.; Wu, B. H.; Yang, J.; Zheng, N. F. Small adsorbate-assisted shape control of Pd and Pt nanocrystals. *Adv. Mater.* **2012**, *24*, 862–879.

[28] Wu, J. B.; Yang, H. Platinum-based oxygen reduction electrocatalysts. *Acc. Chem. Res.* **2013**, *46*, 1848–1857.

[29] Bai, J.; Fang, C. L.; Liu, Z. H.; Chen, Y. A one-pot gold seed-assisted synthesis of gold/platinum wire nanoassemblies and their enhanced electrocatalytic activity for the oxidation of oxalic acid. *Nanoscale* **2016**, *8*, 2875–2880.

[30] Fu, G. T.; Xia, B. Y.; Ma, R. G.; Chen, Y.; Tang, Y. W.; Lee, J. M. Trimetallic PtAgCu@PtCu core@shell concave nanooctahedrons with enhanced activity for formic acid oxidation reaction. *Nano Energy* **2015**, *12*, 824–832.

[31] Gong, M. X.; Li, F. M.; Yao, Z. G.; Zhang, S. Q.; Dong, J. W.; Chen, Y.; Tang, Y. W. Highly active and durable platinum-lead bimetallic alloy nanoflowers for formic acid electrooxidation. *Nanoscale* **2015**, *7*, 4894–4899.

[32] Li, F. M.; Kang, Y. Q.; Peng, R. L.; Li, S. N.; Xia, B. Y.; Liu, Z. H.; Chen, Y. Sandwich-structured Au@polyallylamine@Pd nanostructures: Tuning the electronic properties of the Pd shell for electrocatalysis. *J. Mater. Chem. A* **2016**, *4*, 12020–12024.

[33] Chen, C.; Kang, Y. J.; Huo, Z. Y.; Zhu, Z. W.; Huang, W. Y.; Xin, H. L. L.; Snyder, J. D.; Li, D. G.; Herron, J. A.; Mavrikakis, M. et al. Highly crystalline multimetallic nanoframes with three-dimensional electrocatalytic surfaces. *Science* **2014**, *343*, 1339–1343.

[34] Liu, X. W.; Wang, D. S.; Li, Y. D. Synthesis and catalytic properties of bimetallic nanomaterials with various architectures. *Nanotoday* **2012**, *7*, 448–466.

[35] Porter, N. S.; Wu, H.; Quan, Z. W.; Fang, J. Y. Shape-control and electrocatalytic activity-enhancement of Pt-based bimetallic nanocrystals. *Acc. Chem. Res.* **2013**, *46*, 1867–1877.

[36] Zhang, H.; Jin, M. S.; Xia, Y. N. Enhancing the catalytic and electrocatalytic properties of Pt-based catalysts by forming bimetallic nanocrystals with Pd. *Chem. Soc. Rev.* **2012**, *41*, 8035–8049.

[37] Tan, L. Y.; Li, L. D.; Peng, Y.; Guo, L. Synthesis of Au@Pt bimetallic nanoparticles with concave Au nanocuboids as seeds and their enhanced electrocatalytic properties in the ethanol oxidation reaction. *Nanotechnology* **2015**, *26*, 505401.

[38] Huang, X. Q.; Zhao, Z. P.; Fan, J. M.; Tan, Y. M.; Zheng, N. F. Amine-assisted synthesis of concave polyhedral platinum nanocrystals having {411} high-index facets. *J. Am. Chem. Soc.* **2011**, *133*, 4718–4721.

[39] Xia, B. Y.; Wu, H. B.; Yan, Y.; Lou, X. W.; Wang, X. Ultrathin and ultralong single-crystal platinum nanowire assemblies with highly stable electrocatalytic activity. *J. Am. Chem. Soc.* **2013**, *135*, 9480–9485.

[40] Iyyamperumal, R.; Zhang, L.; Henkelman, G.; Crooks, R. M. Efficient electrocatalytic oxidation of formic acid using Au@Pt dendrimer-encapsulated nanoparticles. *J. Am. Chem. Soc.* **2013**, *135*, 5521–5524.

[41] Devivaraprasad, R.; Ramesh, R.; Naresh, N.; Kar, T.; Singh, R. K.; Neergat, M. Oxygen reduction reaction and peroxide generation on shape-controlled and polycrystalline platinum nanoparticles in acidic and alkaline electrolytes. *Langmuir* **2014**, *30*, 8995–9006.

[42] Higgins, D. C.; Wang, R. Y.; Hoque, M. A.; Zamani, P.; Abureden, S.; Chen, Z. W. Morphology and composition controlled platinum-cobalt alloy nanowires prepared by

electrospinning as oxygen reduction catalyst. *Nano Energy* **2014**, *10*, 135–143.

[43] Nogami, M.; Koike, R.; Jalem, R.; Kawamura, G.; Yang, Y.; Sasaki, Y. Synthesis of porous single-crystalline platinum nanocubes composed of nanoparticles. *J. Phys. Chem. Lett.* **2010**, *1*, 568–571.

[44] Yin, J.; Wang, J. H.; Li, M. R.; Jin, C. Z.; Zhang, T. Iodine ions mediated formation of monomorphic single-crystalline platinum nanoflowers. *Chem. Mater.* **2012**, *24*, 2645–2654.

[45] Eustis, S.; El-Sayed, M. A. Why gold nanoparticles are more precious than pretty gold: Noble metal surface plasmon resonance and its enhancement of the radiative and nonradiative properties of nanocrystals of different shapes. *Chem. Soc. Rev.* **2006**, *35*, 209–217.

[46] Schrinner, M.; Ballauff, M.; Talmon, Y.; Kauffmann, Y.; Thun, J.; Möller, M.; Breu, J. Single nanocrystals of platinum prepared by partial dissolution of Au-Pt nanoalloys. *Science* **2009**, *323*, 617–620.

[47] García-Negrete, C. A.; Rojas, T. C.; Knappett, B. R.; Jefferson, D. A.; Wheatley, A. E. H.; Fernandez, A. Shape-defined nanodimers by tailored heterometallic epitaxy. *Nanoscale* **2014**, *6*, 11090–11097.

[48] Wang, D. S.; Li, Y. D. One-pot protocol for Au-based hybrid magnetic nanostructures via a noble-metal-induced reduction process. *J. Am. Chem. Soc.* **2010**, *132*, 6280–6281.

[49] Lee, J.; Oh, I.; Hwang, S.; Kwak, J. Scanning tunneling microscopy investigation of silver deposition upon Au(111) in the presence of chloride. *Langmuir* **2002**, *18*, 8025–8032.

[50] Li, L. D.; Peng, Y.; Yue, Y. H.; Hu, Y.; Liang, X.; Yin, P. G.; Guo, L. Synthesis of concave gold nanocuboids with high-index facets and their enhanced catalytic activity. *Chem. Commun.* **2015**, *51*, 11591–11594.

[51] Wang, L.; Yamauchi, Y. Autoprogrammed synthesis of triple-layered Au@Pd@Pt core–shell nanoparticles consisting of a Au@Pd bimetallic core and nanoporous Pt shell. *J. Am. Chem. Soc.* **2010**, *132*, 13636–13638.

[52] Personick, M. L.; Langille, M. R.; Zhang, J.; Mirkin, C. A. Shape control of gold nanoparticles by silver underpotential deposition. *Nano Lett.* **2011**, *11*, 3394–3398.

[53] Wanjala, B. N.; Luo, J.; Loukrakpam, R.; Fang, B.; Mott, D.; Njoki, P. N.; Engelhard, M.; Naslund, H. R.; Wu, J. K.; Wang, L. C. et al. Nanoscale alloying, phase-segregation, and core–shell evolution of gold-platinum nanoparticles and their electrocatalytic effect on oxygen reduction reaction. *Chem. Mater.* **2010**, *22*, 4282–4294.

[54] Chen, S. G.; Wei, Z. D.; Qi, X. Q.; Dong, L. C.; Guo, Y. G.; Wan, L. J.; Shao, Z. G.; Li, L. Nanostructured polyaniline-decorated Pt/C@PANI core–shell catalyst with enhanced durability and activity. *J. Am. Chem. Soc.* **2012**, *134*, 13252–13255.

[55] Yang, J.; Ying, J. Y. Nanocomposites of Ag_2S and noble metals. *Angew. Chem., Int. Ed.* **2011**, *50*, 4637–4643.

[56] Wu, Y.; Wang, D. S.; Chen, X. B.; Zhou, G.; Yu, R.; Li, Y. D. Defect-dominated shape recovery of nanocrystals: A new strategy for trimetallic catalysts. *J. Am. Chem. Soc.* **2013**, *135*, 12220–12223.

[57] Wu, J. B.; Qi, L.; You, H. J.; Gross, A.; Li, J.; Yang, H. Icosahedral platinum alloy nanocrystals with enhanced electrocatalytic activities. *J. Am. Chem. Soc.* **2012**, *134*, 11880–11883.

[58] Ilayaraja, N.; Prabu, N.; Lakshminarasimhan, N.; Murugan, P.; Jeyakumar, D. Au-Pt graded nano-alloy formation and its manifestation in small organics oxidation reaction. *J. Mater. Chem. A* **2013**, *1*, 4048–4056.

[59] Fennell, J.; He, D. S.; Tanyi, A. M.; Logsdail, A. J.; Johnston, R. L.; Li, Z. Y.; Horswell, S. L. A selective blocking method to control the overgrowth of Pt on Au nanorods. *J. Am. Chem. Soc.* **2013**, *135*, 6554–6561.

[60] Peng, Z. M.; Yang, H. PtAu bimetallic heteronanostructures made by post-synthesis modification of Pt-on-Au nanoparticles. *Nano Res.* **2009**, *2*, 406–415.

[61] Chen, Y. X.; Heinen, M.; Jusys, Z.; Behm, R. J. Kinetics and mechanism of the electrooxidation of formic acid—Spectroelectrochemical studies in a flow cell. *Angew. Chem., Int. Ed.* **2006**, *45*, 981–985.

[62] Ge, X. B.; Yan, X. L.; Wang, R. Y.; Tian, F.; Ding, Y. Tailoring the structure and property of Pt-decorated nano-porous gold by thermal annealing. *J. Phys. Chem. C* **2009**, *113*, 7379–7384.

[63] Kristian, N.; Yan, Y. S.; Wang, X. Highly efficient submonolayer Pt-decorated Au nano-catalysts for formic acid oxidation. *Chem. Commun.* **2008**, 353–355.

[64] Zhang, D. F.; Li, J.; Kang, J. X.; Chen, T. W.; Zhang, Y.; Wang, L. L.; Guo, L. From Pt-rich dendrites to Ni-rich cuboctahedrons: Structural evolution and electrocatalytic property studies. *CrystEngComm* **2014**, *16*, 5331–5337.

[65] Xu, J. F.; Liu, X. Y.; Chen, Y.; Zhou, Y. M.; Lu, T. H.; Tang, Y. W. Platinum-cobalt alloy networks for methanol oxidation electrocatalysis. *J. Mater. Chem.* **2012**, *22*, 23659–23667.

[66] Zhang, B. W.; Zhang, Z. C.; Liao, H. G.; Gong, Y.; Gu, L.; Qu, X. M.; You, L. X.; Liu, S.; Huang, L.; Tian, X. C. et al. Tuning Pt-skin to Ni-rich surface of Pt_3Ni catalysts supported on porous carbon for enhanced oxygen reduction reaction and formic electro-oxidation. *Nano Energy* **2016**, *19*, 198–209.

[67] Kim, B. J.; Kwon, K.; Rhee, C. K.; Han, J.; Lim, T. H. Modification of Pt nanoelectrodes dispersed on carbon support using irreversible adsorption of Bi to enhance formic acid oxidation. *Electrochim. Acta* **2008**, *53*, 7744–7750.